Global assessment of directional effects in the inter-calibration of optical satellite instruments with the TRUTHS mission

Javier Gorroño, Montserrat Piñol Solé, Nigel Fox, Luis Guanter, Thomas August and Thorsten Fehr

Abstract

Upcoming SI-Traceable Satellite (SITSat) missions such as TRUTHS aim to achieve an unprecented accuracy for SI-traceable measurements of the Earth-reflected radiation. These measurements will support the generation of low uncertainty climate records and significantly improve the calibration of other sensors. In such a context, the uncertainty will be limited by the calibration transfer process rather than the reference sensor. This study presents an end-to-end global inter-calibration simulator capable of assessing the potential uncertainty for multiple scenarios that considers the interrelation of different error sources and match-ups. We first define the sensor-to-sensor match-ups through an orbital analysis that is followed by a top-of-atmosphere (TOA) radiance modelling of each match-up. Finally, we calculate the radiometric uncertainty based on different error sources combined globally. In this first implementation we have calculated the match-ups of TRUTHS against observations by the Copernicus Sentinel-2A satellite over land areas throughout a year. We calculate the angular mismatch for both viewing differences and solar changes from different overpass time. We define multiple inter-calibration scenarios based on temporal, angular or cloud constraints. These first results show that considering overpasses up to 15 minute difference, low cloud probability and matching field-of-view (FoV), within 5°, we sample most land areas with a mean error <0.1% and bias regression <0.5%. We have also restricted the sun zenith angle (SZA) to 60° to minimise solar angle and viewing azimuthal dispersion over the poles. This also results in data-gaps of several months that might be complemented with dedicated manouevres or a dedicated processing of these polar-region match-ups.

I. Introduction

The last decade has seen the development of missions such as TRUTHS (Traceable Radiometry Underpinning Terrestrial and Helio-Studies [1]) and CLARREO (Climate Absolute Radiance and Refractivity Observatory [2]), now implemented as a NASA pathfinder mission [3], designed explicitly to provide highly accurate and trusted SI(Système international)-traceable climate records. These missions were also designed with the specific intent to provide 'in-space' reference calibration to other optical satellite sensors to improve their performance and interoperability. In recognition of this new class of sensor the Committee on Earth Observation Satellites (CEOS) and World Meteorological Organisation Global Space Inter-calibration System (WMO-GSICS) have created the name SITSat (SI-Traceable Satellite) together with an associated formal definition [4].

The TRUTHS mission achieves and evidences its low SI-traceable uncertainty through regular re-calibration of its hyperspectral Imaging Spectrometer (HIS), on-board, directly linked to a space-borne primary reference standard, a Cryogenic Solar Absoluter Radiometer (CSAR). The On-Board Calibration System (OBCS) provides tunable spectrally-resolved radiation that can be distributed between the CSAR, where its power is measured, and the HIS where the now known power is transformed to radiance illuminating and calibrating the HIS. The process can be considered a space adapted mimic of a terrestrial calibration in a national metrology institute. The CSAR is a space adaptation of the terrestrial cryogenic radiometer which has served as the primary SI standard of choice for nearly 40 years [5]. TRUTHS is

J. Gorroño and Luis Guanter are with the Research Institute of Water and Environmental Engineering (IIAMA) at Universitat Politècnica de València, 46022 Valencia, Spain.

Montserrat Piñol Solé, Thomas August and Thorsten Fehr are with the European Space Agency, Keplerlaan 1, 2201 AZ Noordwijk, Netherlands

Nigel Fox is with the National Physical Laboratory, Hampton Road, Teddington, Middlesex, TW11 0LW, UK

currently in the Phase B2 implementation phase as an ESA Earthwatch mission funded by a consortium of member states led by UK in partnership with Switzerland, Greece, Romania, Czech Republic and Spain with a target launch date in 2030. The mission has a design goal to globally and continuously measure Earth reflected spectral radiance from 320 to 2400 nm with a spectral resolution of 4-8 nm, ground sampling distance of 50 m and uncertainty goal of 0.3% (k=2). In practice due to data volume constraints the full spatial resolution is likely to be limited to specific targets, in particular those used for calibration of other sensors, such as the CEOS reference sites [6].

The upcoming SITSat missions such as TRUTHS, will constitute a system that not only enables harmonization but the establishment of SI-traceability and performance enhancement. In preparation for such a scenario where the reference sensor does not limit the uncertainty of an inter-calibration process, the study and correction of sources of errors related to the calibration transfer process e.g. spatial and temporal mismatch, becomes highly relevant.

One of the first broad studies of the error sources associated with satellite inter-calibration identified eight dimensions when matching two spacecraft in orbit and studied several of these and their impact on a calibration against the proposed CLARREO mission [7]. Similarly, the work in [8] studied the effect of spectral responses, spectral resolution, spectral filter shift, geometric misregistrations, and spatial resolutions. This work also introduced a combined uncertainty of the different effects with final figures that represent overall bounds on the achievable uncertainty estimate. Later work in [9] studies the uncertainty in the spectral, spatial and temporal dimensions associated with an inter-calibration with TRUTHS mission as a reference sensor. The study effectively describes the contributions as an error distribution rather than bounds of uncertainty. However, the combination of them does not include all the potential dimensions in the inter-calibration. Further work has been carried out in different studies but exploring each of the dimensions independently [10], [11], [12], [13], [14].

The orbit definition for the TRUTHS mission is another critical step since it defines the number of match-ups with the target sensor, their locations and angular configuration among others. A conventional sun-synchronous orbit flying in close time tandem to another specific satellite could clearly have near continuous match-up opportunities within the tandem time delay window. However, satellites outside of this window, other than Geo-stationary satellites, would rarely if ever have time optimized match-ups. An orbital model that identifies the match-ups between CLARREO and sun-synchronous polar orbital sensors such as CERES (Clouds and the Earth's Radiant Energy System) or VIIRS (Visible Infrared Imaging Radiometer Suite) is presented in [15]. The work not only identifies the valid match ups between the sensors but it also discusses the number of potential samples required to achieve the climate quality uncertainty in the inter calibration, considering the relatively low instantaneous signal-to-noise ratio (SNR) of CLARREO (nb, observations are intended to be spatially and temporally averaged reducing sensitivity to single pixel SNR). However, the study does not consider all the potential uncertainty sources and the correlation among them in a global context.

The interrelation between different errors (i.e. error correlation) is a factor in deriving an appropriate combined estimate of the potential radiometric uncertainty that could be attributed to the inter-calibration process. The general assumption of an uncorrelated scenario (i.e. quadratic summation of different uncertainty contributions) is not necessarily correct and a case by case scenario must be carefully assessed. Furthermore, the inter-calibration methods generally require the accumulation of different sensor-to-sensor match-ups. This requires the development of a methodology that is capable of defining the achievable accuracy based on an error distribution from which an uncertainty estimate can be derived.

This study defines and implements an end-to-end inter-calibration simulator that is capable of assessing the potential uncertainty on a case by case basis for multiple inter-calibration scenarios. Here we aim to connect the orbit sampling, the specific scene modelling of each sensor-to-sensor match-up and the combination of different error sources at a global level. In a way, we are aiming to generate a digital twin prototype for inter-calibration studies. For this first study, we present the uncertainty introduced due to angular mismatch between the TRUTHS mission and the target reference over land areas. These angular differences can be introduced by differences in satellite viewing angles but also in different solar illumination angles introduced by the delay between satellite overpasses. Furthermore, these angular differences can result in top-of-atmosphere (TOA) radiance errors coming from both surface and atmospheric angular sensitivity.

The general inter-calibration methodology aims at measuring ideally identical targets by two sensors with the same view at the same time and possessing similar spatial and spectral responses (e.g. GSICS [16], [17] or CLARREO [2]). For polar orbiting satellites, this is generally possible through satellite manoeuvres that align the angular configuration of the TRUTHS sensor to the target satellite if they differ from a nominal nadir view.

These satellite manoeuvres can reduce directionality errors to a negligible level. However, they require a complex tasking, consume the satellite energy resources and have an impact on the main TRUTHS mission goal (i.e. provide benchmark measurements of both incoming solar radiation and outgoing reflected radiation). Therefore, this study explores a complementary approach that considers near-simultaneous overpasses of both nadir and view angle mismatched observations but does not include satellite manoeuvres. This implies potentially larger instantaneous errors but ones that are expected to reduce with accumulation of different crossings (angles and scenes) over the year.

In this manuscript, the selected target mission is the Copernicus Sentinel 2 (S2). The Copernicus S2 satellite mission currently consists of two satellites (S2A and S2B) that together sample the Earth with better than a 5-day revisit. Its main payload instrument measures in 13 spectral bands spanning the visible, near-infrared (VNIR) and the shortwave infrared (SWIR) at spatial resolutions of 10, 20 or 60 m [18].

The specific study of the angular mismatch supports both the definition of an orbit and pointing strategy for the TRUTHS mission that optimises the inter-calibration accuracy with minimum impact on the global benchmark accuracy. The continuous development of this simulator is expected to become the basis for the definition of an inter-calibration strategy for the TRUTHS mission and/or similar optical instruments.

The manuscript is structured in two sections consisting of methodology (Section II) and results (Section III). Section II is subdivided into a definition of the end-to-end general framework (subsection II-A), the orbit definition and match-up data (subsection II-B) and the modelling of TOA radiance including both the scene surface and atmosphere (subsection II-C). Section III first describes the distribution of sensor-to-sensor match-ups based on parameters such as time differences, latitude or angular distribution. It then provides the results of the inter-calibration uncertainty assessment for each considered scenario.

II. Methodology

A. General framework

The general idea of the proposed methodology is that of simulating the end-to-end process of the inter-calibration at a global scale. That is, we aim to use the orbital projections to generate all the resultant match-ups between two sensors and the associated characteristics of their observations that impact the match-up uncertainty. We could refer to this as an observational digital-twin for inter-calibration studies. The logic of this concept is represented in Figure 1.

[Fig. 1 about here.]

The left end of the schema includes the *orbit match-up generator* and the *match-up products database*. The former provides location and angular information at the event (detailed discussion in subsection II-B) whereas the second ingests the relevant information to model the surface bidirectional reflectance factor (BRDF) and the atmosphere. These two are fundamental information for the module *TOA radiance modelling* used to generate a realistic TOA radiance scene at each sensor-to-sensor match-up (detailed discussion in subsection II-C). The following module, *error match-up generator* aims to assess the effect of spectral response mismatch, spatial response mismatch, scene/cloud dynamics, polarisation or angular mismatch. In this study, we have implemented the angular mismatch which is assessed by managing the call to the *TOA radiance modelling*. Specifically, we call the module for each sensor-to-sensor match-up with specific viewing angular information and timestamp for TRUTHS and S2A overpasses respectively.

The result of this process is an error that is iteratively produced at each sensor-to-sensor match-up and managed by the *global post-processing assessment*. In this first implementation, the global assessment is based on an analysis of the error distribution and the fitting of the radiance curve that are discussed in Section III. The implementation has been applied to three different scenarios defined as:

- *Relaxed scenario* (Subsection III-B). This scenario only discards sensor-to-sensor match-ups with a sun zenith angle (SZA) higher than 60° or a time difference between sensors larger than 15 minutes.
- *Intermediate scenario* (Subsection III-C). This scenario further filters out the previous match-ups by constraining S2A field-of-view (FoV) (here simplified to 5° viewing zenith angle (VZA)) matching the TRUTHS FoV. It also filters out the matches by considering low probability cloud events (further info in subsection II-C).
- *Restrictive scenario* (Subsection III-D). This latter scenario restricts the matches from the previous case by decreasing the maximum delay between sensors to just 5 minutes and only considers angle matching below 2 degrees.

  The tighter criteria for ray-tacing in the third scenario are tending towards GSICS collocation practices, where so far larger experience with low Earth orbit (LEO) sensors [17] has been made in the thermal infrared.

B. Orbit analysis

TRUTHS satellite mission will be launched into a non-sun-synchronous orbit with an inclination of 90 degrees and an average geodetic altitude of 611 km. Sentinel-2 orbit is sun-synchronous with 10:30 Local Time at Descending Node, an average geodetic altitude of 800.9 km and an inclination of 98.6 deg.

Due to the difference in altitude between both satellites, TRUTHS and Sentinel-2 will overtake each other frequently, with a period of about 1.8 days. The TRUTHS orbital plane will rotate with respect to the Sun and will complete a full revolution after 1 year. During the periods of the year when the orbital plane is close to the orbital plane of sensors in sun-synchronous orbits, co-observations (without manoeuvres) may be possible at latitudes other than polar regions. The TRUTHS Mean Local Solar Time at Ascending Node Crossing on the 1st of January has been set to 17:00h, which corresponds to approximately RAAN 356°.

The methodology to identify collocated observations between TRUTHS sensor with 100km-wide swath and Sentinel-2 MSI instrument is outlined below and illustrated in Figure 2:

- Sentinel-2 swath contour is split with a step of 5 seconds (green rectangles)
- TRUTHS swath is split in across-track direction with a granularity of 10 km (blue lines)
- the intersection of each intermediate TRUTHS swath line with the rectangular portions of Sentinel-2 swath will result in 2 points
- from those 2 resulting points, the viewing geometry angles (SAA, SZA, VAA, OZA) and timestamp to TRUTHS and Sentinel-2 are calculated and used for further analysis.

[Fig. 2 about here.]

C. Top-of-atmosphere radiance modelling

The TOA radiance modelling is generated with the Library for Radiative Transfer (LibRadtran) [19], [20]. We parameterise the scene (surface, atmosphere and geometry) and obtain an output result that represents the convolved radiance into a spectral response function (SRF). In this implementation, we have selected the SRF of the Moderate Resolution Imaging Spectroradiometer (MODIS) bands 2 (approx 841-876 nm spectral interval), 3 (approx 459-479 nm spectral interval) and 6 (approx 1628-1652 nm spectral interval) to keep consistency with the selected BRDF surface products [21].

As mentioned in the previous paragraph, we have selected the MCD43 products [22]. The product describes the BRDF using the RossThick-LiSparseReciprocal kernels obtained from an inversion of a semiempirical model over 16 days of MODIS directional surface reflectance data. The three kernel values (fiso , fvol , fgeo) can be used in Libradtran to estimate the surface anisotropic effects [23], [24]. Specifically, we have used daily L3 Global 30ArcSec CMG V006 products for MODIS bands 2, 3 and 6 [25] from year 2021. These BRDF kernels are then introduced as part of the input parameterisation of the Libradtran radiative transfer software. If the product does not contain a retrieval value, we search for and iterate at 5-day intervals from the acquisition day up to a maximum of 20 days difference. In case there is no valid result at any of these days, we use the default BRDF associated to an IGBP landclass in Libradtran. The IGBP landclass is obtained at each sensor-to-sensor match-up from MCD12C products [26] hosted in Google Earth Engine (GEE) [27].

The geometry configuration is based on the angular configuration for each satellite overpass at the match-up points given by the orbital simulation (see subsection II-B). This information is complemented by the altitude given by a digital elevation model at 0.1° spatial resolution [28].

The aerosol optical thickness (AOT) is modelled from the Copernicus Atmosphere Monitoring Service (CAMS) Global Near-Real-Time [29], [30] from the European Centre for Medium-Range Weather Forecasts (ECMWF) and hosted in GEE. The forecast value for the closest hour, day, and location, is selected. In case no valid value is found or the connection with the server is lost, the value will be retrieved from an AOT with the monthly average from March 2019 to March 2020 at a 0.1° spatial resolution[31]. In the unlikely scenario that both approaches fail, a default value of 0.2 will be allocated. Other properties of the AOT are modelled with the default values: rural type aerosol in the boundary layer, background aerosol above 2 km and spring-summer conditions [19], [20].

The water vapour (WV) is obtained from Global Forecast System (GFS) 384-Hour Predicted Atmosphere Data produced by National Oceanic and Atmospheric Administration (NOAA) and hosted in GEE. Similarly to the AOT, the closest value for the closest 6-hour forecast sample is selected. In the absence of a value or invalid retrieval, WV maps with monthly average values from March 2019 to March 2020 at a 0.1° spatial resolution will be accessed [32]. If both the two previous methods report an unsuccessful result, we allocate a value of 1 cm. From the same GFS product, we also extract a forecast value of cloud probability in the pixel area defined as 27830×27830 meters.

The atmospheric profile is set to mid-latitude summer with a representative wavelength absorption parameterization (REPTRAN model [33]) customised for MODIS bands to be consistent with the BRDF products. The radiative transfer runs with 16 streams and the DISORT solver.

Figure 3 represents the viewing error modelled for inclinations up to 20 degrees for the considered MODIS bands. It also describes the temporal error as a consequence of the sun's movement with delays of $\pm$ 30 minutes from the overpass time. The overpass represents a typical S2A overpass at latitude -23.6002 and longitude 15.11956 that coincides with the CEOS RadCalNet Gobabeb site [34]. The specific overpass time is 09h:17m:02s for the 25th of November 2021. The atmosphere has been modelled with an AOT 0.14, WV of 1.694 cm and altitude of 510 m.

[Fig. 3 about here.]

This example indicates the relatively significant level of error, exceeding the 1% value, that occur for viewing angle differences larger than TRUTHS FoV (5°). This viewing error also varies as function of spectral band. The directionality of MODIS B3 is dominated by the Rayleigh scattering whereas MODIS B6 shows a nearly symmetric result from nadir with a visible anisotropy due to the hotspot right at the edge of the polar plot. It also shows that these B6 errors have an important azimuthal dependence mostly separated by the backward and forward scattering properties of the surface.

Similarly, Figure 4 illustrates the temporal variations for the same example as in Figure 3.

[Fig. 4 about here.]

The temporal variations show important variations but to a lesser extent than the viewing impact. The temporal error tends to by highly linear for time delays below 30 minutes. Again, there is an important difference depending on the spectral band that for the 15 minute threshold can range from 0.5% in MODIS

B6 to over 1% in MODIS B3. Thus, the coupling of both surface and atmosphere proves very critical in order to simulate a correct balance between the two effects.

III. Results

A. Orbit match-ups and parameters

The orbit analysis described in Section II-B results in a set of timestamp, location and angular information for both the S2A and TRUTHS mission over a year. The analysis is only restricted to 15 minutes so that further filtering and analysis can select the optimum sensor-to-sensor matches for each scenario.

In general, the time difference between the two missions shows a nearly uniform and symmetric distribution (mean value below 20 seconds for all cases). The long repeat cycle of the TRUTHS mission (61 days; see subsection II-B) as compared to the 10 days repeat cycle of S2A results in a diverse number of opportunities with different angular and temporal conditions. This potentially leads towards a more symmetric distribution of the time delays between the two sensors in a match-up area. The *intermediate scenario* produces the most symmetric distribution (mean value below 5 seconds) likely explained by the constraining of the S2A FoV to 5°, matching that of TRUTHS FoV.

Figure 5 includes the polar distribution of solar and viewing angles for different scenarios. The location of the sensor-to-sensor match-ups is displayed in subsections 7, 9 and 11. The considered scenarios are: *all*, *relaxed intermediate*. The former refers to all the sensor-to-sensor match-ups over sunlit land areas whereas the latter two scenarios where defined at the end of Section I.

[Fig. 5 about here.]

The polar plot of the angle distribution indicates that without a general restriction on the SZA, a large fraction of crossings would occur at very high SZA over the poles. In that case, not only the large SZA would be challenging but also the viewing azimuthal differences between TRUTHS and S2A. The TRUTHS orbit is designed as a true 90° polar orbit whereas the S2A orbit has a slight inclination of 98.62°. Thus, the restriction to a SZA lower than 60°in the *relaxed scenario* significantly reduces both the solar angle and the viewing azimuthal dispersion. The *intermediate scenario* shows that a 15-minute threshold between mission overpasses still results in important solar angle differences between TRUTHS and S2A. However, this is partially compensated because these angular differences do not visually indicate a correlated nature.

The temporal distribution of these opportunities over the year is also an important criterion since any calibration effort ideally requires a continuous effort assessment, dependent on drift of the target sensor and any sub-orbital variations. Figure 6 depicts the same sensor-to-sensor match-ups as a function of day of the year and the latitude.

[Fig. 6 about here.]

As explained in subsection II-B, the rotation of the TRUTHS orbital plane with respect to the Sun results in a yearly pattern. Combined with a general criterion of a SZA threshold of 60° to avoid large angular effects in polar regions, results in an approximate two-month period of match-ups followed by a four-month of no valid opportunities.

B. Results for a relaxed scenario: SZA<60°and Δ t<15'

As explained in Section I, this scenario considers all match-ups with the only conditions being that the SZA is lower than 60° and the time difference is lower than 15 minutes. Figure 7 presents the match-ups across the globe with a colour bar indicating the level of error for each sample. These same errors are presented as an error distribution and radiance linear regression in Figure 8.

[Fig. 7 about here.]

[Fig. 8 about here.]

The maps show a good distribution of coincidences that cover a range of biomes, latitudes and longitudes. However, there are specific areas like the Sahara desert or the Amazon forest that are not covered due to the orbit configuration selected for this analysis. Using other orbit RAAN assumption or performing the simulation over other years (due to the relative phasing between S2 and TRUTHS) would have yielded match-ups over Sahara/Amazon areas. Several of the stripes are long enough to infer an evolution of the viewing angles through the orbit that is illustrated through a gradient of colour at each stripe.

Most of the errors are contained within 5% and the error standard deviation is between 2-3%. However, the distribution in all cases presents a slight asymetric distribution that is translated in mean error values of 0.5-1% The fitted radiance curve for B2 and B6 shows a slight overestimation that in the case of B6 represents a significant bias. This bias for B6 can be explained by the error resulting from high radiance values of S2A. High radiance values tend to be close to the swath edge of S2A and the hot-spot area of the surface reflectance (see Figure 3c). These higher radiance values create an imbalance in the curve fitting that could explain the higher bias. B3 results in a lower bias but higher offset both in absolute and relative terms. Conversely, this might indicate that the relative angular error is nearly constant through the radiance range likely explained by the more symmetric nature of the B3 surface error (see Figure 3b)

C. Results for an intermediate scenario: matching FoV and cloud screening

This *intermediate scenario* narrows down the number of sensor-to-sensor matches by matching both S2A and TRUTHS FoV and only considering those opportunities that are likely to be cloud-free.

Figure 9 presents the matches for this scenario.

[Fig. 9 about here.]

It is clearly visible that the number of opportunities has significantly decreased. However, it still covers a large number of areas across the globe. It is interesting to note how most of the crossings over tropical regions are mostly not present due to their high cloud probability (e.g. central Africa or Borneo island).

Figure 10 reports the error distribution and radiance linear regression for this scenario.

[Fig. 10 about here.]

The standard deviation of the angular errors has been reduced to the range 1-2%. More importantly, the error distribution is now almost symmetric with just a small mean error of 0.1% for B3. This can be explained because we are now matching TRUTHS and S2 FoV results in a symmetric and reciprocal angular sampling. Together with a nearly uniform delay distribution, constrains the error propagation and results to a symmetric error distribution of TOA radiance biases.

This has been directly translated in a better fitting for B2 and B6 but not so for B3 (see Figures 10d, 10e and 10f). In the latter case, the spectral band is highly influenced by atmospheric directionality and matching FoVs does not represent a significant improvement.

D. Results for a restrictive scenario: matching angles and Delta t<5'

This scenario sets up highly restrictive conditions in order to select the "best" sensor-to-sensor matches in terms of angular match.

Following on from the previous *intermediate scenario*, we have further reduced the maximum time delay between missions to five minutes and selected matching angles with less than 2°. This matching angle is defined as:

$$\begin{aligned}&\arccos(\cos(VZA_{TRUTHS})\cdot\cos(VZA_{S2A})\\&\cdot\cos(VAA_{TRUTHS}-VAA_{S2A})+\sin(VZA_{TRUTHS})\\&\cdot\sin(VZA_{S2A}))\leq 2^{\circ}\end{aligned}\tag{1}$$

where VAA represents the viewing azimuth angle.

Figure 11 represents the global matches with the associated error to each of them. Note that due to the low number of opportunities and low error value, the scales have been significantly increased and the colour bar has been reduced to a range of $\pm 1\%$.

[Fig. 11 about here.]

The map indicates that most of sensor-to-sensor matches have been lost with matches concentrated in 9 cluster areas. For example, there are no matches in the entire continents of Africa and Oceania. It should of course be noted that small changes in selected orbit configurations of both TRUTHS and indeed S2 (reflecting small anular changes) can have a significant impact on the locations of match-ups and so the above should be seen as illustrative.

Figure 12 displays the error distribution and radiance curve fitting for this scenario.

[Fig. 12 about here.]

The error distribution shows again a very small mean error (below the 0.1%) but significantly decreases the error dispersion with a standard deviation of 0.3%. On the contrary, the lower radiance dynamic range and small number of samples does not improve (or even worsens) the curve radiance fitting. Thus, this scenario indicates these samples can be used as ”golden points” in order to constrain an inter-comparison but are not sufficient for a more detailed characterisation e.g. large radiance range or location dependence.

IV. Discussion

A. General comments

We have presented a novel study that seeks to define an optimum inter-calibration strategy for the TRUTHS mission based on an end-to-end global simulation (or ”inter-calibration digital twin”). The general methodology described in subsection II-A defines an orbit match-up analysis that is the input to a TOA radiance modelling of the event where the combination of different error sources at a global level results in an integrated performance assessment of the intercalibration.

For this first study, we present the error introduced due to angular mismatch (both satellite viewing angles and solar angles) between the TRUTHS mission and the S2A satellite over land. We have defined a general scenario (*all*) and three different scenarios (named *relaxed intermediate* and *restrictive*) that refer to different temporal, angular or cloud constraints.

Subsection III-A indicates that the restriction to a SZA lower than 60 $^\circ$ significantly reduces both the solar angle and the viewing azimuthal dispersion. However, Figure 6 suggests that it will also lead to significant periods with no sensor-to-sensor match-ups for the three proposed scenarios.

The results for the *relaxed scenario* report a high number of opportunities but results in a mean error distribution at the 0.5-1%. The fitted radiance also presents a significant bias that for surface effects as in B6 can be explained by the impact of anisotropic high radiance values of S2A.

The results for the *intermediate scenario* report a lower number of opportunities but still a good coverage of different areas across the globe. However, the introduction of cloud probability generates a more realistic simulation of potential match-ups and indicate how crossings over tropical regions mostly disappear. Thus, it suggest that the definition of an orbit (e.g. RAAN 0 ± 5 $^\circ$) might result in a majority of crossings over desert areas or tropical forests with a direct consequence on the number of cloud-free opportunities. This scenario clearly improves the mean error distribution to a value below 0.1% that is translated into an improvement of the curve fitting for bands dominated by surface effects (MODIS B2 and B6).

Finally, the results for the *restrictive scenario* result in the lowest angular match-up error (standard deviation below 0.3%) but at the cost of a very small number of opportunities. This is sufficient to broadly check the inter-calibration at every event but does not allow a characterisation in terms of radiance range, location dependency or focal plane variations. However, for some sensors which contain their own on-board calibration/monitoring systems this may still be adequate, particularly if they can also be supplemented by other targets and/or sensors that may also have been calibrated by TRUTHS independently.

Based on these preliminary findings, a potential optimum global strategy utilising only this methodology could be that of selecting an *intermediate scenario* as a baseline approach due to its large number of sensor-to-sensor match-ups, large radiance dynamic range and a negligible bias due to angular effects (see Figures 9 and 10). This can be complemented with a *restrictive scenario* (here they are a subset of an *intermediate scenario*) that could be used as an anchor point. Nonetheless, this approach would result in significant temporal gaps of approximately four months as presented in Figure 6. In order to complement these time gaps, dedicated manouevres could be scheduled during these periods depending on the mission needs. Alternatively, the sensor-to-sensor match-ups over these polar regions could be considered at the cost of larger directional errors and/or specific angular corrections.

As indicated above for the full TRUTHS calibration system we will likely have an integrated calibration system of systems, utilizing a range of methods to cover the range of observational conditions, including all those currently in use, summarized on the CEOS CalVal portal [35] but enhanced by a TRUTHS reference calibration from space.

B. Adapting to other scenarios

The same code can be adapted to model different scenarios that are not either global or an inter-calibration between two sensors in space.

For example, this code has been adapted to model in-situ targets such as RadCalNet [34] where TRUTHS will be used to transfer its high accuracy calibration to anchor the network which in turn will then provide on-going calibrations to other sensors. The example presented in Figure 3 has been modelled based on the RadCalNet Gobabeb typical site conditions. Similarly, as for the scenarios presented here, the opportunities throughout the year have been identified and translated into angular mismatch error. In this specific case, these angular errors might be partially compensated by including a BRDF correction due to its in-situ calculation. In the future we will extend the analysis to consider geo-stationary satellites and of course aircraft sensors or an ad-hoc validation campaign. However, in all cases it is important that we test the validity of these simulations against real data. At the time of writing, there are no hyperspectral sensors with global coverage and full polar orbit. In the absence of a perfectly matching data, alternatives such as S2 vs. EnMAP or similar combinations could be explored.

This study has only been based on land areas with no consideration of ocean sensor-to-sensor match-ups. By including ocean opportunities we would be distorting the results since most of the sensor-to-sensor match-ups are at extremely low radiance values where effects such as noise, polarisation or straylight will be most relevant. Thus, we consider it best to pursue the ocean case as a separate analysis for specific ocean focused missions e.g. those used for Ocean colour.

Similarly to the ocean case, cloudy scenes have not been considered but filtered out assuming a cloud cover criterion. In order to consider them for the inter-calibration, a specific criterion must be set that is based on the cloud dynamics and scene uniformity. Future studies should look into this specific match-ups which could enlarge the number of opportunities and the dynamic range of the sensor-to-sensor inte-calibration (particularly in the case of a *restrictive scenario* subsection III-D).

Finally, we have made the comparison in terms of radiance for the scenarios here presented here. This is useful if we are directly comparing the radiance calibration between TRUTHS and a target sensor over a large radiance dynamic range. However, there is the option to compare these results in terms of reflectance which is straightforward with the code presented here.

C. Further work

The approach presented here is under continuous evolution and is expected to include several new features and refinements as the mission moves into an operational phase. The obvious next step is to include the other sources of error such as spectral and spatial mismatch but also polarization.

Current modelling of the BRDF relies on the use of MODIS MCD43D products. They are sufficiently realistic to model patterns of surface directionality but improvements will be considered as a trade-off with memory and processing requirements. For example, the use of quality flags in separate products MCD43D31-MCD43D41 would select the best products and also allow alternative BRDF products to be considered if necessary. The atmospheric modelling is mostly based on AOT and WV products. However other type of information such as type of aerosol can also be envisaged.

The current band modelling in terms of REPTRAN MODIS bands significantly reduces the computing requirements. It could be possible to consider a hyperspectral implementation that would imply the parsing of several more BRDF bands and the execution of the radiative transfer with a smaller band resolution. This would not only allow a hyperspectral assessment of the angular effect but would also allow the blend of this effect with the spectral response one [9].

This study has successfully considered the cloud cover by setting a 20% cloud probability threshold based on forecast values in a pixel area of $27830\times$ 27830 meters. An alternative would be that of modelling the cloud probability based on the closest overpass of Sentinel 2 or Landsat missions. This approach would provide a high-spatial resolution (20-30m as compared to 50-100 m of TRUTHS spatial resolution) but other effects might arise such as the quality of the cloud detection algorithm or the constant local time overpass. Even more important is the consideration of clouds dynamics and general scene changes for example by including a simple transport model of the high-spatial resolution cloud.

The current prototype runs on a HP DL380P G9 server with 2 x Intel Xeon E5-2690 V4 (14 cores) and 128GB RAM. This is sufficient to run each MODIS band in approximately 2 hours. However, all the potential improvements mentioned here will require an improvement of the processing resources as well as software optimisation so as not to exponentially increase the running time.

D. Conclusion

In conclusion, we have illustrated here through our simulator how the new SITSat class of sensor like TRUTHS will provide the means to revolutionise future decades of satellite earth observation. Providing, as a free and open service, the capability to improve the performance and interoperability of optical satellite imager data products through in-orbit reference calibration directly traceable to a certifiable SI-Traceable reference.

The new system of systems enabled by such calibrations will enhance climate and other science and commercial applications facilitating increased trust in their derived information. The implementation of calibration methodologies illustrated in this paper will benefit not only public sector space agencies but also most importantly the ‘new space’ providers where the ability to have their own on-board calibration/monitoring systems is rarely possible.

Acknowledgments

This study has been funded by ESA TMAC contract.

V. References Section

References

[1] N. Fox and P. Green, “Traceable radiometry underpinning terrestrial- and helio-studies (truths): An element of a space-based climate and calibration observatory,” *Remote Sensing*, vol. 12, no. 15, 2020. [Online]. Available: https://www.mdpi.com/2072-4292/12/15/2400

[2] B. A. Wielicki, D. F. Young, M. G. Mlynczak, K. J. Thome, S. Leroy, J. Corliss, J. G. Anderson, C. O. Ao, R. Bantges, F. Best, K. Bowman, H. Brindley, J. J. Butler, W. Collins, J. A. Dykema, D. R. Doelling, D. R. Feldman, N. Fox, X. Huang, R. Holz, Y. Huang, Z. Jin, D. Jennings, D. G. Johnson, K. Jucks, S. Kato, D. B. Kirk-Davidoff, R. Knuteson, G. Kopp, D. P. Kratz, X. Liu, C. Lukashin, A. J. Mannucci, N. Phojanamongkolkij, P. Pilewskie, V. Ramaswamy, H. Revercomb, J. Rice, Y. Roberts, C. M. Roithmayr, F. Rose, S. Sandford, E. L. Shirley, W. L. Smith, B. Soden, P. W. Speth, W. Sun, P. C. Taylor, D. Tobin, and X. Xiong, “Achieving climate change absolute accuracy in orbit,” *Bulletin of the American Meteorological Society*, vol. 94, no. 10, pp. 1519 – 1539, 2013. [Online]. Available: https://journals.ametsoc.org/view/journals/bams/94/10/bams-d-12-00149.1.xml

[3] Y. Shea, G. Fleming, G. Kopp, C. Lukashin, P. Pilewskie, P. Smith, K. Thome, B. Wielicki, X. Liu, and W. Wu, "Clarreo pathfinder: Mission overview and current status," in *IGARSS 2020 - 2020 IEEE International Geoscience and Remote Sensing Symposium*, 2020, pp. 3286–3289.

[4] H. Boesch, H. Brindley, F. Carminati, N. Fox, D. Helder, T. Hewison, D. Houtz, S. Hunt, G. Kopp, M. Mlynczak, T. S. Pagano, H. Revercomb, E. Richard, P. Rosenkranz, Y. Shea, S. Simis, D. Smith, T. C. Stone, W. Sun, J. Xiong, B. Wielicki, H. Yang, and X. Ye, "Si-traceable space-based climate observation system: a ceos and gsics workshop, national physical laboratory, london, uk, 9-11 sept 2019," Other 10.47120/npl.9319, January 2022. [Online]. Available: http://eprintspublications.npl.co.uk/9319/

[5] J. E. Martin, N. P. Fox, and P. J. Key, "A cryogenic radiometer for absolute radiometric measurements," *Metrologia*, vol. 21, no. 3, p. 147, jan 1985. [Online]. Available: https://dx.doi.org/10.1088/0026-1394/21/3/007

[6] G. Chander, T. J. Hewison, N. Fox, X. Wu, X. Xiong, and W. J. Blackwell, "Overview of intercalibration of satellite instruments," *IEEE Transactions on Geoscience and Remote Sensing*, vol. 51, no. 3, pp. 1056–1080, 2013.

[7] B. A. Wielicki, D. R. Doelling, D. F. Young, N. G. Loeb, D. P. Garber, and D. G. MacDonnell, "Climate quality broadband and narrowband solar reflected radiance calibration between sensors in orbit," in *IGARSS 2008 - 2008 IEEE International Geoscience and Remote Sensing Symposium*, vol. 1, Conference Proceedings, pp. I–257–I–260.

[8] G. Chander, D. Aaron, N. Mishra, and A. Shrestha, "Assessment of spectral, misregistration, and spatial uncertainties inherent in the cross-calibration study," *IEEE Transactions on Geoscience and Remote Sensing*, vol. 51, pp. 1282–1296, 03 2013.

[9] J. Gorroño, A. C. Banks, N. P. Fox, and C. Underwood, "Radiometric inter-sensor cross-calibration uncertainty using a traceable high accuracy reference hyperspectral imager," *ISPRS Journal of Photogrammetry and Remote Sensing*, vol. 130, pp. 393–417, 2017. [Online]. Available: http://www.sciencedirect.com/science/article/pii/S0924271616306517

[10] C. Lukashin, B. A. Wielicki, D. F. Young, K. Thome, J. Zhonghai, and S. Wenbo, "Uncertainty estimates for imager reference inter-calibration with clarreo reflected solar spectrometer," *Geoscience and Remote Sensing, IEEE Transactions on*, vol. 51, no. 3, pp. 1425–1436, 2013.

[11] W. Sun and C. Lukashin, "Modeling polarized solar radiation from the ocean–atmosphere system for clarreo inter-calibration applications," *Atmospheric Chemistry and Physics*, vol. 13, no. 20, pp. 10 303–10 324, 2013. [Online]. Available: https://www.atmos-chem-phys.net/13/10303/2013/

[12] W. Sun, R. R. Baize, C. Lukashin, and Y. Hu, "Deriving polarization properties of desert-reflected solar spectra with parasol data," *Atmospheric Chemistry and Physics*, vol. 15, no. 13, pp. 7725–7734, 2015. [Online]. Available: https://www.atmos-chem-phys.net/15/7725/2015/

[13] A. Wu, X. Xiong, Z. Jin, C. Lukashin, B. N. Wenny, and J. J. Butler, "Sensitivity of intercalibration uncertainty of the clarreo reflected solar spectrometer features," *IEEE Transactions on Geoscience and Remote Sensing*, vol. 53, no. 9, pp. 4741–4751, 2015.

[14] W. Wu, X. Liu, X. Xiong, Y. Li, Q. Yang, A. Wu, S. Kizer, and C. Cao, "An accurate method for correcting spectral convolution errors in intercalibration of broadband and hyperspectral sensors," *Journal of Geophysical Research: Atmospheres*, vol. 123, no. 17, pp. 9238–9255, 2018. [Online]. Available: https://agupubs.onlinelibrary.wiley.com/doi/abs/10.1029/2018JD028585

[15] C. M. Roithmayr, C. Lukashin, P. W. Speth, G. Kopp, K. Thome, B. A. Wielicki, and D. F. Young, "Clarreo approach for reference intercalibration of reflected solar sensors: On-orbit data matching and sampling," *IEEE Transactions on Geoscience and Remote Sensing*, vol. 52, no. 10, pp. 6762–6774, 2014.

[16] M. Goldberg, G. Ohring, J. Butler, C. Cao, R. Datla, D. Doelling, V. Gärtner, T. Hewison, B. Iacovazzi, D. Kim, T. Kurino, J. Lafeuille, P. Minnis, D. Renaut, J. Schmetz, D. Tobin, L. Wang, F. Weng, X. Wu, F. Yu, P. Zhang, and T. Zhu, "The global space-based inter-calibration system," *Bulletin of the American Meteorological Society*, vol. 92, no. 4, pp. 467 – 475, 2011. [Online]. Available: https://journals.ametsoc.org/view/journals/bams/92/4/2010bams2967_1.xml

[17] T. J. Hewison, X. Wu, F. Yu, Y. Tahara, X. Hu, D. Kim, and M. Koenig, "Gsics inter-calibration of infrared channels of geostationary imagers using metop/iasi," *IEEE Transactions on Geoscience and Remote Sensing*, vol. 51, no. 3, pp. 1160–1170, 2013.

[18] M. Drusch, U. Del Bello, S. Carlier, O. Colin, V. Fernandez, F. Gascon, B. Hoersch, C. Isola, P. Laberinti, P. Martimort, A. Meygret, F. Spoto, O. Sy, F. Marchese, and P. Bargellini, "Sentinel-2: Esa's optical high-resolution mission for gmes operational services," *Remote Sensing of Environment*, vol. 120, pp. 25–36, 2012, the Sentinel Missions - New Opportunities for Science. [Online]. Available: https://www.sciencedirect.com/science/article/pii/S0034425712000636

[19] C. Emde, R. Buras-Schnell, A. Kylling, B. Mayer, J. Gasteiger, U. Hamann, J. Kylling, B. Richter, C. Pause, T. Dowling, and L. Bugliaro, "The libradtran software package for radiative transfer calculations (version 2.0.1)," *Geoscientific Model Development*, vol. 9, no. 5, pp. 1647–1672, 2016. [Online]. Available: https://gmd.copernicus.org/articles/9/1647/2016/

[20] B. Mayer and A. Kylling, "Technical note: The libradtran software package for radiative transfer calculations - description and examples of use," *Atmospheric Chemistry and Physics*, vol. 5, no. 7, pp. 1855–1877, 2005. [Online]. Available: https://acp.copernicus.org/articles/5/1855/2005/

[21] X. Xiong, A. Angal, K. A. Twedt, H. Chen, D. Link, X. Geng, E. Aldoretta, and Q. Mu, "Modis reflective solar bands on-orbit calibration and performance," *IEEE Transactions on Geoscience and Remote Sensing*, vol. 57, no. 9, pp. 6355–6371, 2019.

[22] A. H. Strahler, W. Lucht, C. Schaaf, T. Tsang, F. Gao, and J.-P. Muller, "Modis brdf / albedo product : Algorithm theoretical basis document version 5 . 0," 1999.

[23] J.-L. Roujean, M. Leroy, and P.-Y. Deschamps, "A bidirectional reflectance model of the earth's surface for the correction of remote sensing data," *Journal of Geophysical Research: Atmospheres*, vol. 97, no. D18, pp. 20 455–20 468, 1992. [Online]. Available: https://agupubs.onlinelibrary.wiley.com/doi/abs/10.1029/92JD01411

[24] W. Wanner, X. Li, and A. H. Strahler, "On the derivation of kernels for kernel-driven models of bidirectional reflectance," *Journal of Geophysical Research: Atmospheres*, vol. 100, no. D10, pp. 21 077–21 089, 1995. [Online]. Available: https://agupubs.onlinelibrary.wiley.com/doi/abs/10.1029/95JD02371

[25] C. Schaaf and Z. Wang, "Mcd43d04-9 and mcd43d016-18 modis/terra+aqua brdfalbedo parameter1, 2 and 3 for band2, 3 and 6 daily l3 global 30arcsec cmg v006 [data set]. nasa eosdis land processes distributed active archive center," https://doi.org/10.5067/MODIS/MCD43D04.006;https://doi.org/10.5067/MODIS/MCD43D05.006;https://doi.org/10.5067/MODIS/

MCD43D06.006;https://doi.org/10.5067/MODIS/MCD43D07.006;https://doi.org/10.5067/MODIS/MCD43D08.006;https://doi.org/10.5067/MODIS/MCD43D09.006;https://doi.org/10.5067/MODIS/MCD43D16.006;https://doi.org/10.5067/MODIS/MCD43D17.006;https://doi.org/10.5067/MODIS/MCD43D18.006, 2015, [Accessed 2024-03-26].

[26] M. Friedl and D. Sulla-Menashe, "Modis/terra+aqua land cover type yearly l3 global 0.05deg cmg v061 [data set]. nasa eosdis land processes distributed active archive center." https://doi.org/10.5067/MODIS/MCD12C1.061, [Accessed 2024-03-26].

[27] N. Gorelick, M. Hancher, M. Dixon, S. Ilyushchenko, D. Thau, and R. Moore, "Google earth engine: Planetary-scale geospatial analysis for everyone," *Remote Sensing of Environment*, vol. 202, pp. 18–27, 2017, big Remotely Sensed Data: tools, applications and experiences. [Online]. Available: https://www.sciencedirect.com/science/article/pii/S0034425717302900

[28] N. E. O. team and M. A. S. Team., "Srtm digital elevation model," https://neo.gsfc.nasa.gov/view.php?datasetId=SRTM_RAMP2_TOPO, [Accessed 2024-03-26].

[29] A. Benedetti, J.-J. Morcrette, O. Boucher, A. Dethof, R. J. Engelen, M. Fisher, H. Flentje, N. Huneeus, L. Jones, J. W. Kaiser, S. Kinne, A. Mangold, M. Razinger, A. J. Simmons, and M. Suttie, "Aerosol analysis and forecast in the european centre for medium-range weather forecasts integrated forecast system: 2. data assimilation," *Journal of Geophysical Research: Atmospheres*, vol. 114, no. D13, 2009. [Online]. Available: https://agupubs.onlinelibrary.wiley.com/doi/abs/10.1029/2008JD011115

[30] ——, "Aerosol analysis and forecast in the european centre for medium-range weather forecasts integrated forecast system: 2. data assimilation," *Journal of Geophysical Research: Atmospheres*, vol. 114, no. D13, 2009. [Online]. Available: https://agupubs.onlinelibrary.wiley.com/doi/abs/10.1029/2008JD011115

[31] N. E. O. team and M. A. S. Team., "Aerosol optical thickness (1 month - terra/modis)," https://neo.gsfc.nasa.gov/view.php?datasetId=MODAL2_M_AER_OD, [Accessed 2024-03-26].

[32] ——, "Water vapor (1 month - terra/modis)," https://neo.gsfc.nasa.gov/view.php?datasetId=MODAL2_M_SKY_WV, [Accessed 2024-03-26].

[33] J. Gasteiger, C. Emde, B. Mayer, R. Buras, S. Buehler, and O. Lemke, "Representative wavelengths absorption parameterization applied to satellite channels and spectral bands," *Journal of Quantitative Spectroscopy and Radiative Transfer*, vol. 148, pp. 99–115, 2014. [Online]. Available: https://www.sciencedirect.com/science/article/pii/S0022407314002842

[34] M. Bouvet, K. Thome, B. Berthelot, A. Bialek, J. Czapla-Myers, N. P. Fox, P. Goryl, P. Henry, L. Ma, S. Marcq, A. Meygret, B. N. Wenny, and E. R. Woolliams, "Radcalnet: A radiometric calibration network for earth observing imagers operating in the visible to shortwave infrared spectral range," *Remote Sensing*, vol. 11, no. 20, 2019. [Online]. Available: https://www.mdpi.com/2072-4292/11/20/2401

[35] P. Castracane and T. Storm, "Ceos cal/val portal," 2024, [Online; accessed 19/04/2024]. [Online]. Available: https://calvalportal.ceos.org/

List of Figures

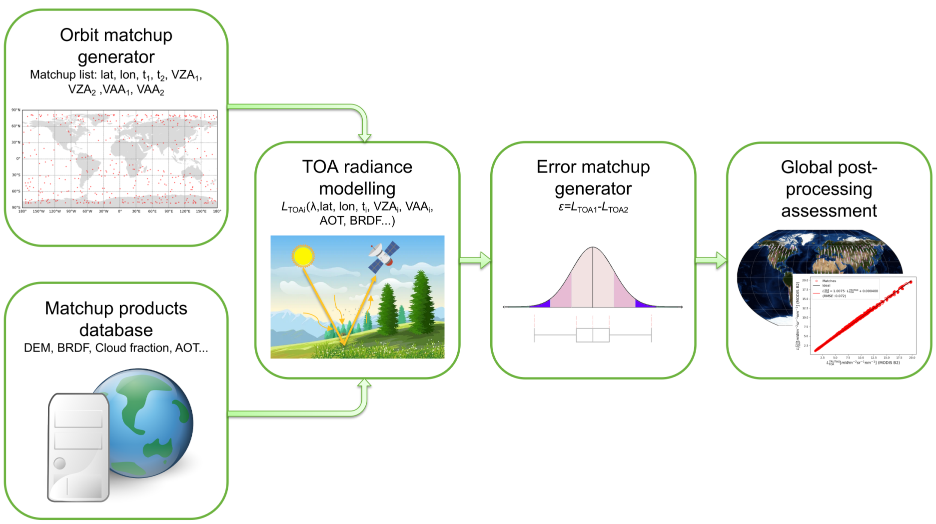

Fig. 1. Workflow schema of the TRUTHS inter-calibration assessment based on global realistic simulations.

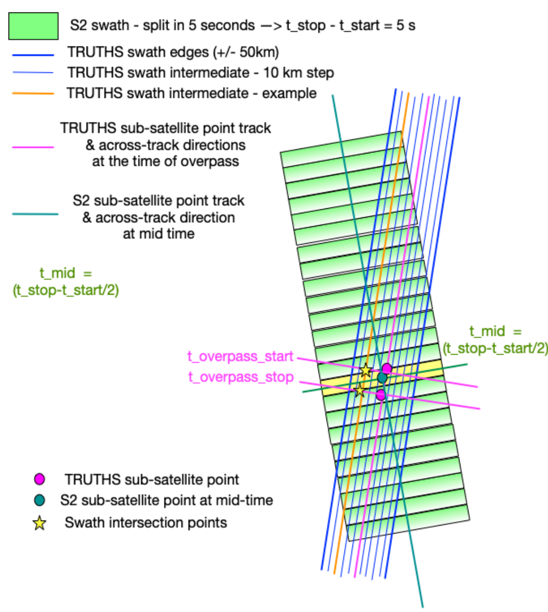

Fig. 2. Schematic representation of the orbit modelling to generate the TRUTHS vs. S2A matches accross the globe.

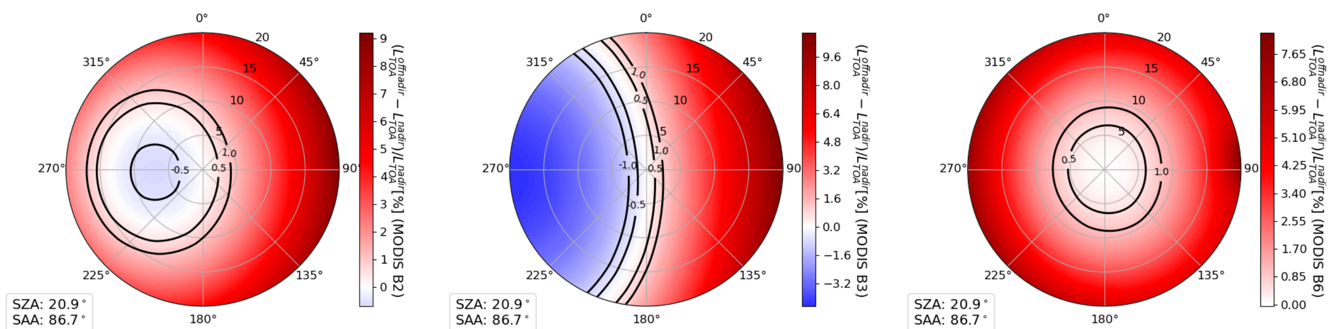

(a) MODIS B2 (860nm) (b) MODIS B3 (460nm) (c) MODIS B6 (1640nm)

Fig. 3. TRUTHS viewing error modeled for inclinations up to 20 degrees for MODIS bands B2 (860nm; Figure 3a), B3 (460nm; Figure 3b) and B6 (1640nm; Figure 3c).

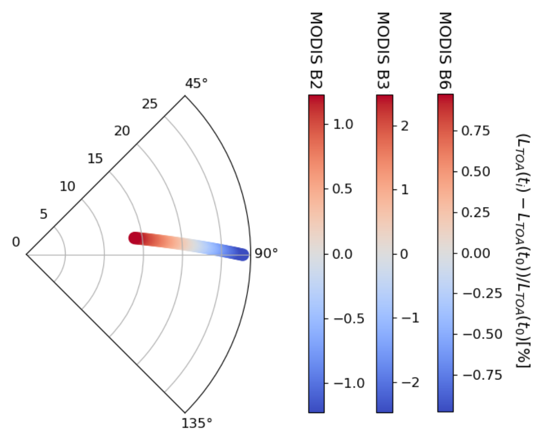

Fig. 4. TRUTHS solar angle evolution and radiometric error modeled for temporal delays up to $\pm$ 30 minutes from the overpass time and MODIS bands B2, B3 and B6.

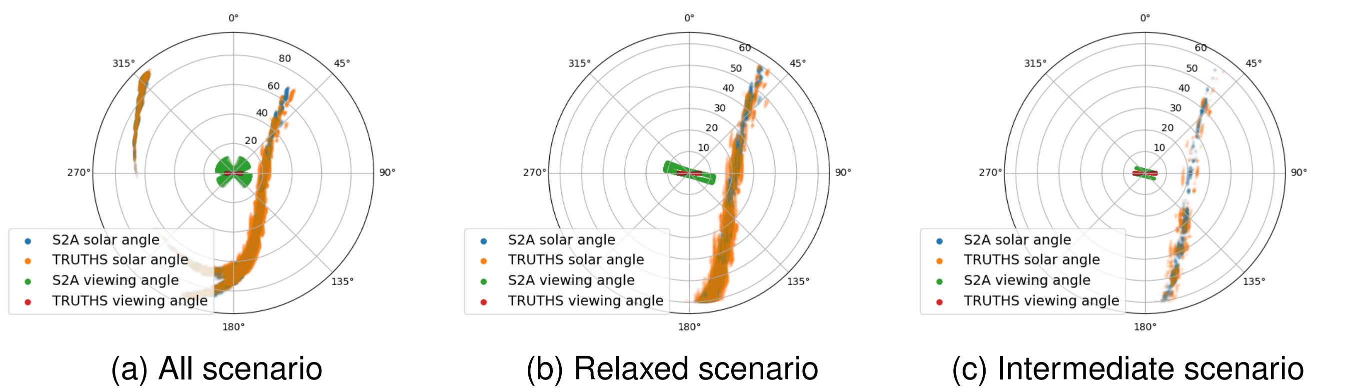

Fig. 5. TRUTHS vs. S2A sensor-to-sensor match-up polar distribution of angles for 3 different scenarios: *all* (Figure 5a), *relaxed* (Figure 5b) and *intermediate* scenarios (Figure 5c).

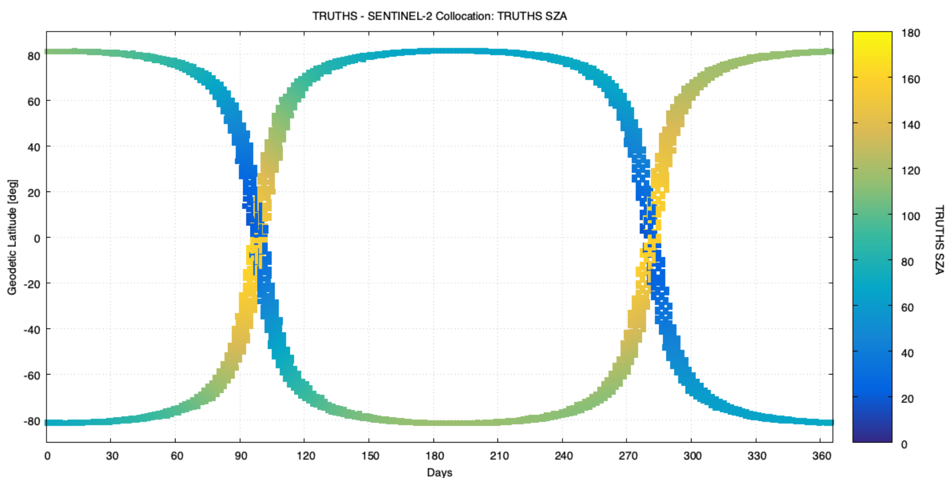

Fig. 6. Collocation opportunities TRUTHS - S2A as a function of the day of the year and considering actual swaths for TRUTHS and S2.

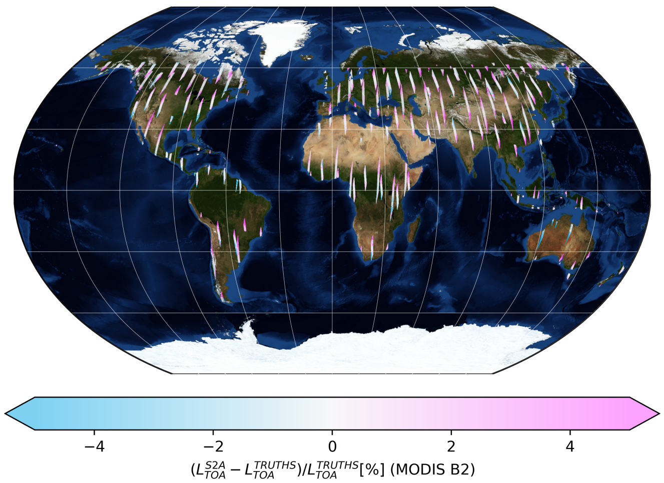

(a) MODIS B2 (860nm)

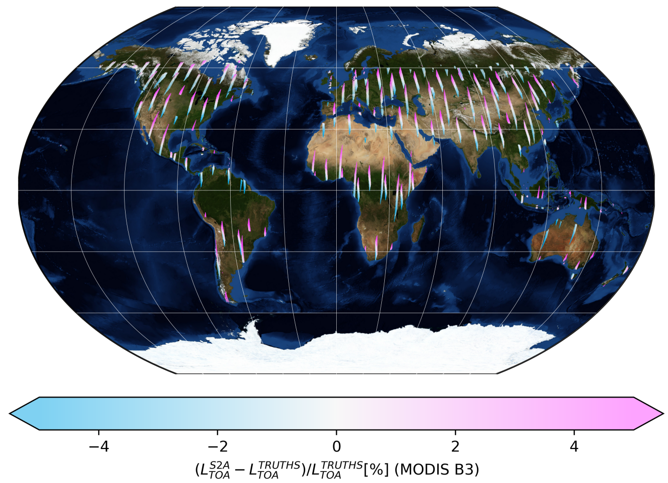

(b) MODIS B3 (460nm)

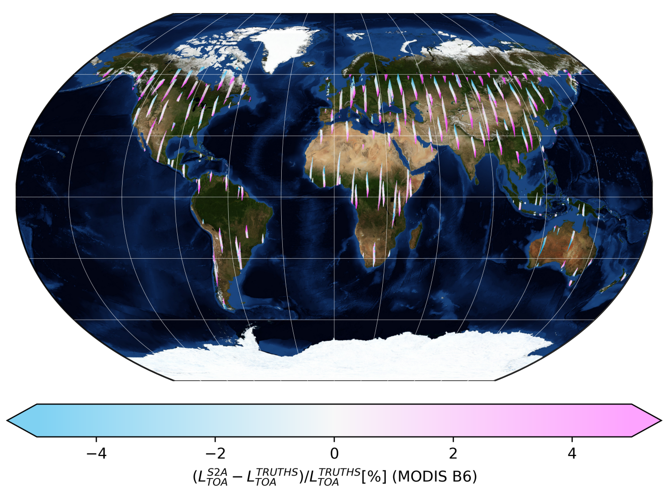

(c) MODIS B6 (1640nm)

Fig. 7. TRUTHS vs. S2A angular error over the Earth projection considering a *relaxed scenario* for MODIS bands B2 (860nm; Figure 7a), B3 (460nm; Figure 7b) and B6 (1640nm; Figure 7c).

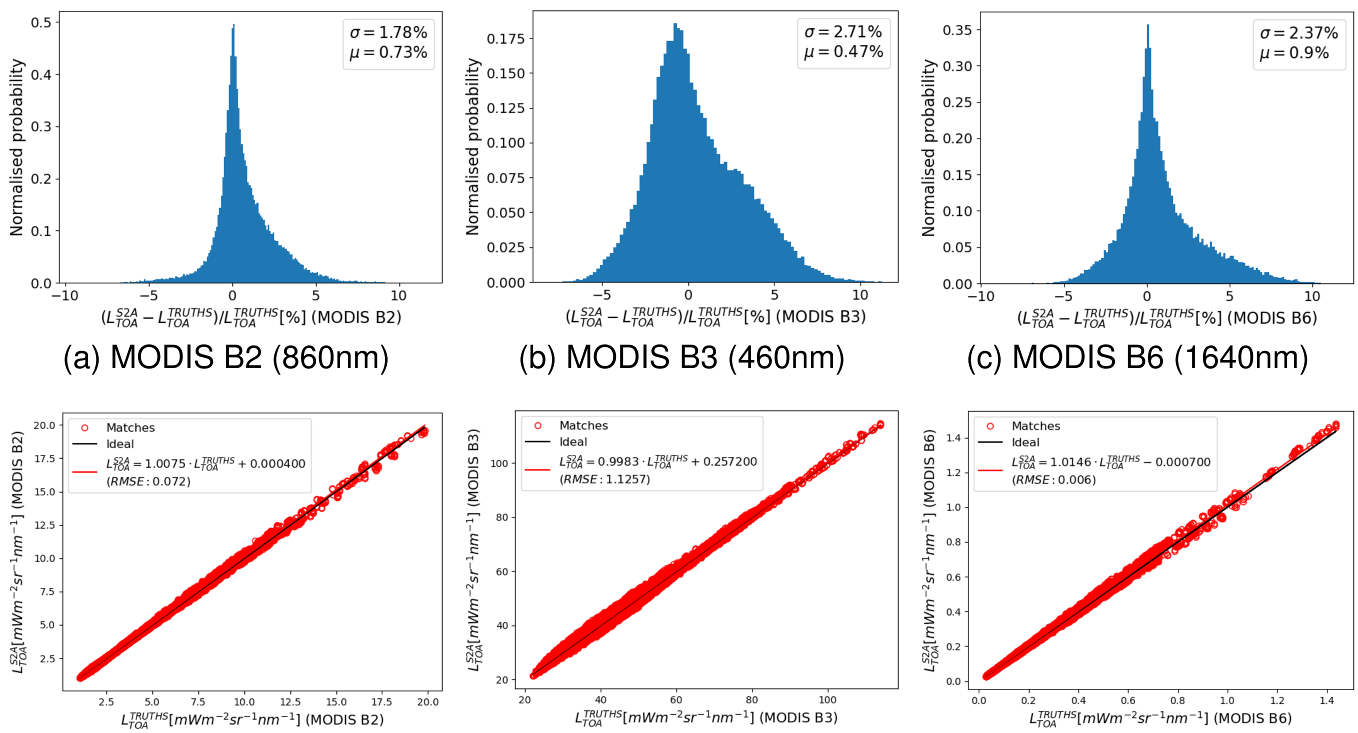

(a) MODIS B2 (860nm) (b) MODIS B3 (460nm) (c) MODIS B6 (1640nm)

(d) MODIS B2 (860nm) (e) MODIS B3 (460nm) (f) MODIS B6 (1640nm)

Fig. 8. TRUTHS vs. S2A angular error distribution considering a *relaxed scenario* for MODIS bands B2 (860nm; Figure 8a), B3 (460nm; Figure 8a) and B6 (1640nm; Figure 8a) and radiance regression the same three MODIS bands (Figures 8d, 8e and 8f)

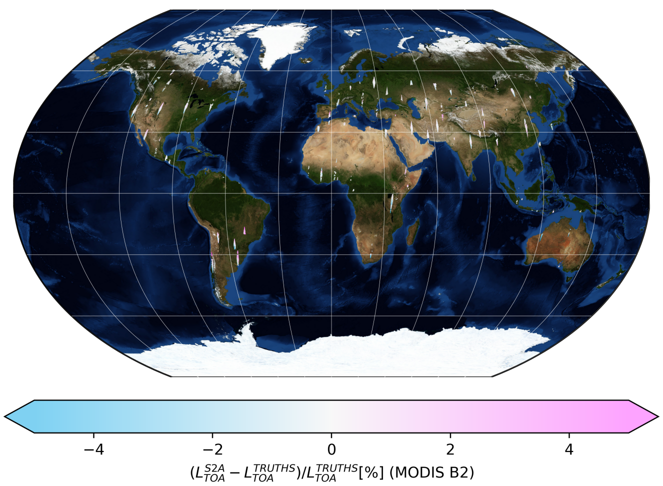

(a) MODIS B2 (860nm)

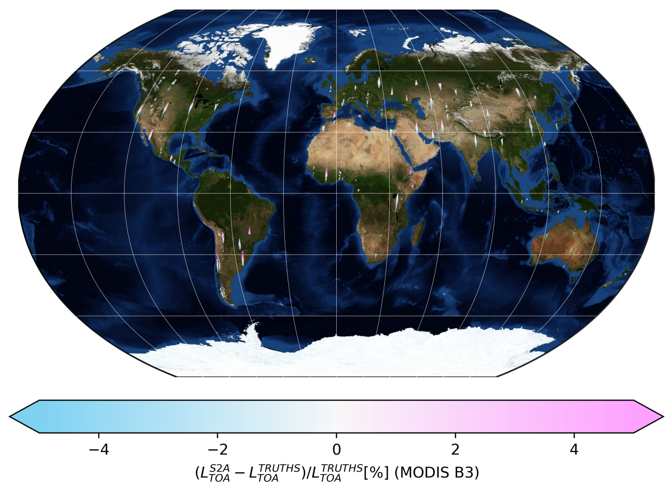

(b) MODIS B3 (460nm)

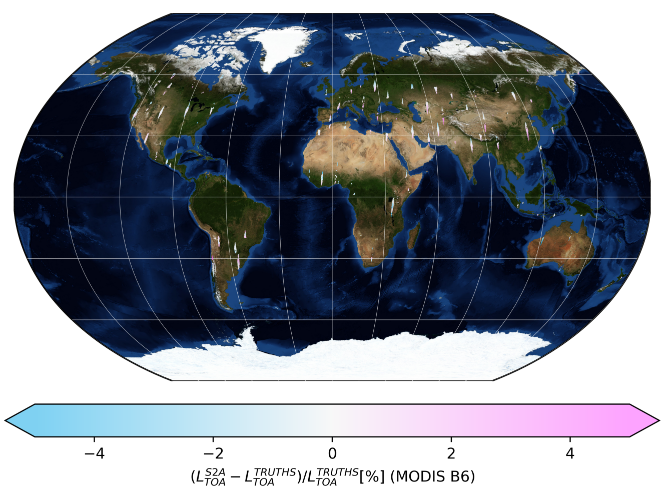

(c) MODIS B6 (1640nm)

Fig. 9. TRUTHS vs. S2A angular error over the Earth projection considering a *intermediate scenario* for MODIS bands B2 (860nm; Figure 9a), B3 (460nm; Figure 9b) and B6 (1640nm; Figure 9c).

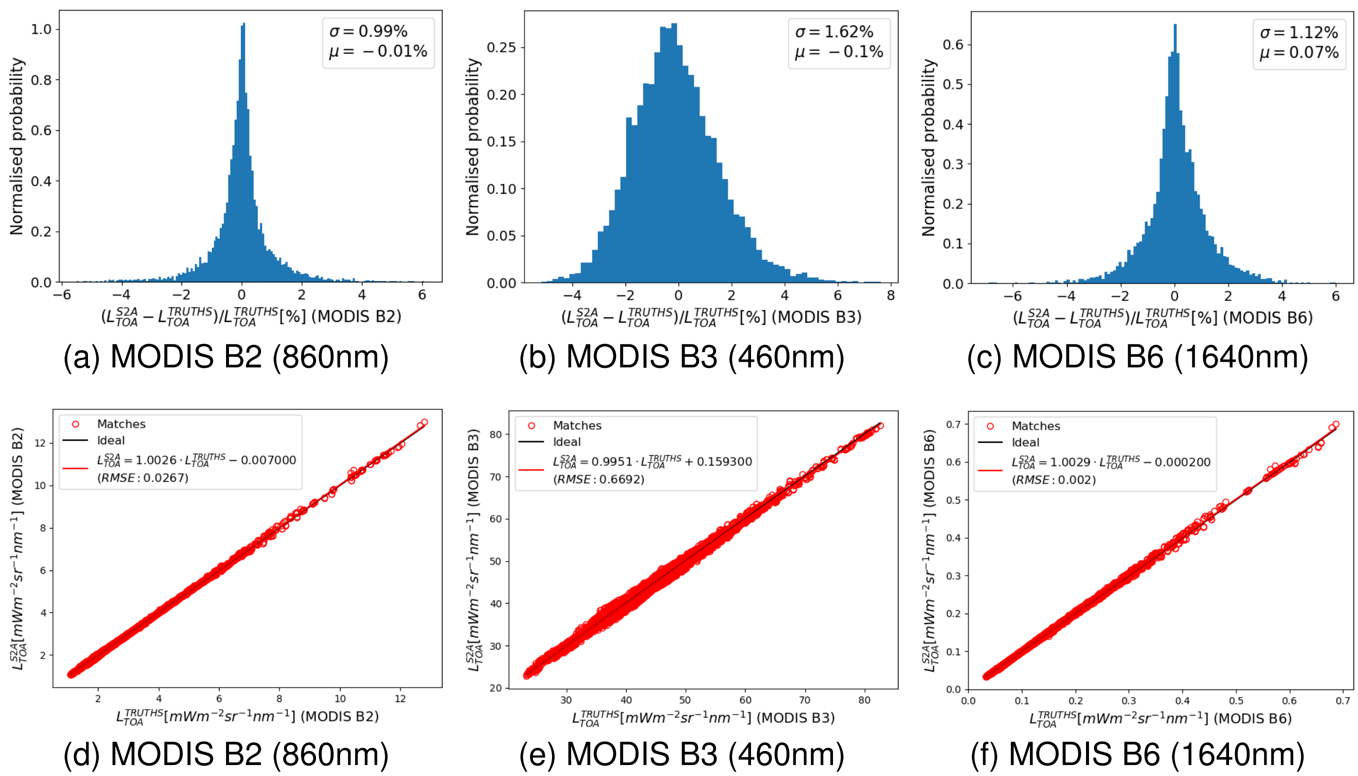

Fig. 10. TRUTHS vs. S2A angular error distribution considering a *intermediate scenario* for MODIS bands B2 (860nm; Figure 10a), B3 (460nm; Figure 10b) and B6 (1640nm; Figure 10c) and radiance regression the same three MODIS bands (Figures 10d, 10e and 10f)

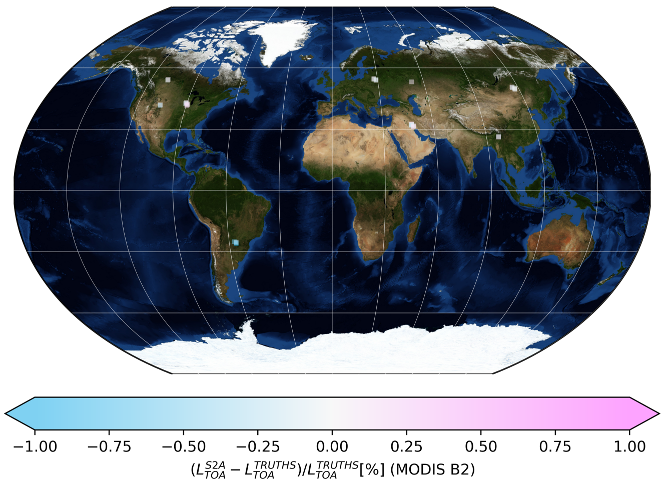

(a) MODIS B2 (860nm)

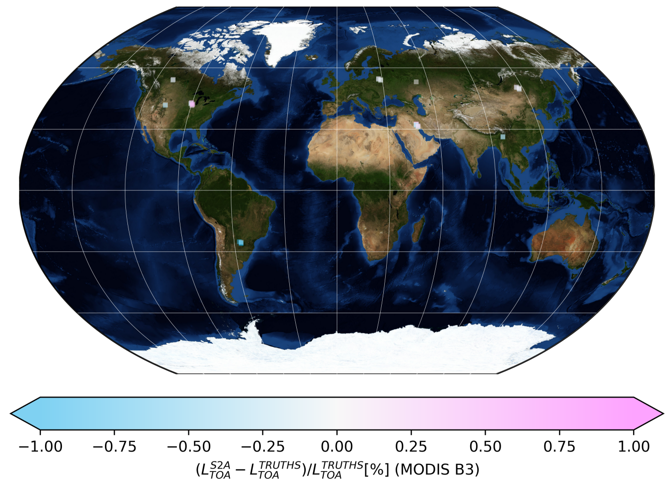

(b) MODIS B3 (460nm)

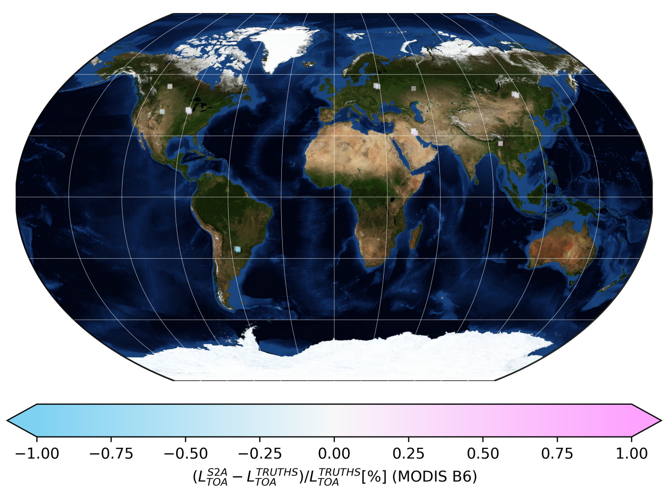

(c) MODIS B6 (1640nm)

Fig. 11. TRUTHS vs. S2A angular error over the Earth projection considering a *restrictive scenario* for MODIS bands B2 (860nm; Figure 11a), B3 (460nm; Figure 11b) and B6 (1640nm; Figure 11c).

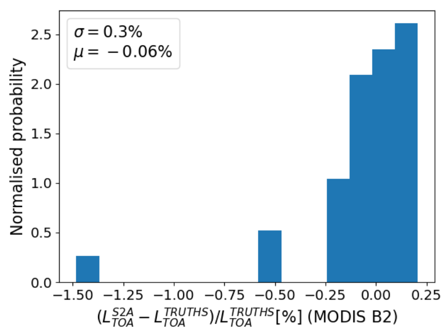

(a) MODIS B2 (860nm)

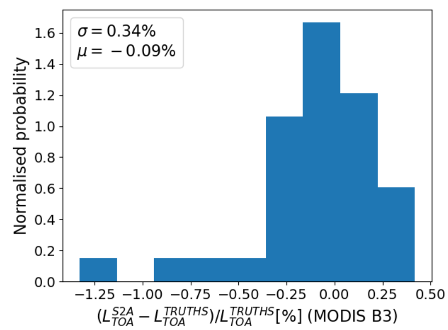

(b) MODIS B3 (460nm)

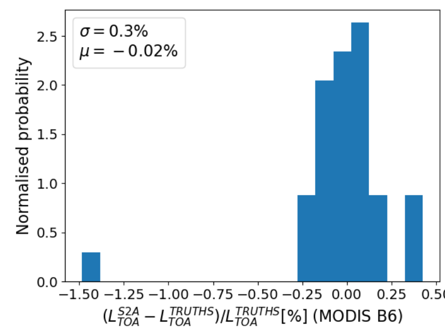

(c) MODIS B6 (1640nm)

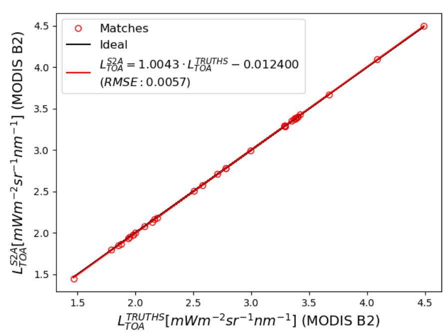

(d) MODIS B2 (860nm)

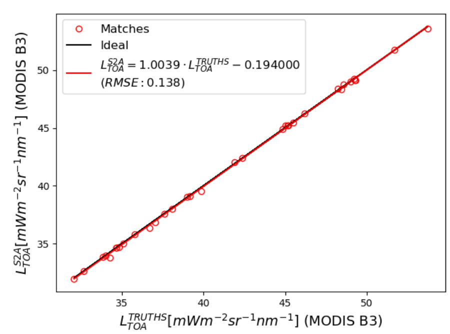

(e) MODIS B3 (460nm)

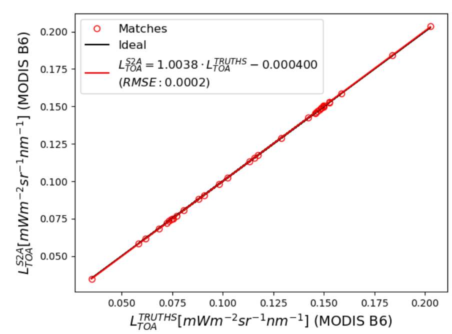

(f) MODIS B6 (1640nm)

Fig. 12. TRUTHS vs. S2A angular error distribution considering a *restrictive scenario* for MODIS bands B2 (860nm; Figure 12a), B3 (460nm; Figure 12b) and B6 (1640nm; Figure 12c) and radiance regression the same three MODIS bands (Figures 12d, 12e and 12f). The markers in this illustration have been exaggerated for visual purposes as well as a lower colour bar range